Electronic Supplementary Material (ESI) for Inorganic Chemistry Frontiers.

Supporting Information

Graphite@Silicon embedded in Carbon Conformally Coated Tiny SiO_2 Nanoparticles Matrix for High-Performance Lithium-Ion Batteries

Huitian Liu[a], Xu Liu[a], Zhaolin Liu[b], Junyan Tao[a], Xiaoqian Dai[a], Qi Yang[a], Jikai Xu[a], Zhongqiang Shan[a,*]

[a]School of Chemical Engineering and Technology, Tianjin University, Tianjin 300350, China

[b] Institute of Materials Research and Engineering (IMRE), A*STAR (Agency for Science, Technology and Research), 2 Fusionopolis Way, Innovis #08-03, 138634, Singapore.

E-mail: shanzq@tju.edu.cn

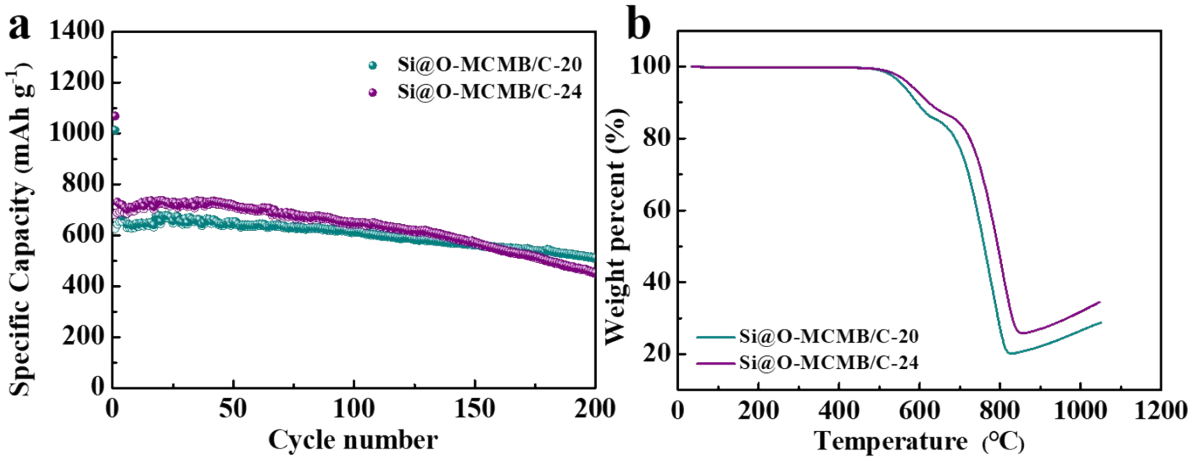

Figure S1 (a) Cycling performances of Si@O-MCMB/C with different Si contents. (b) TGA curves under an oxygen atmosphere, where the Si@O-MCMB/C composites with 20 and 24 wt% Si content are denoted as Si@O-MCMB/C-20 and Si@O-MCMB/C-24.

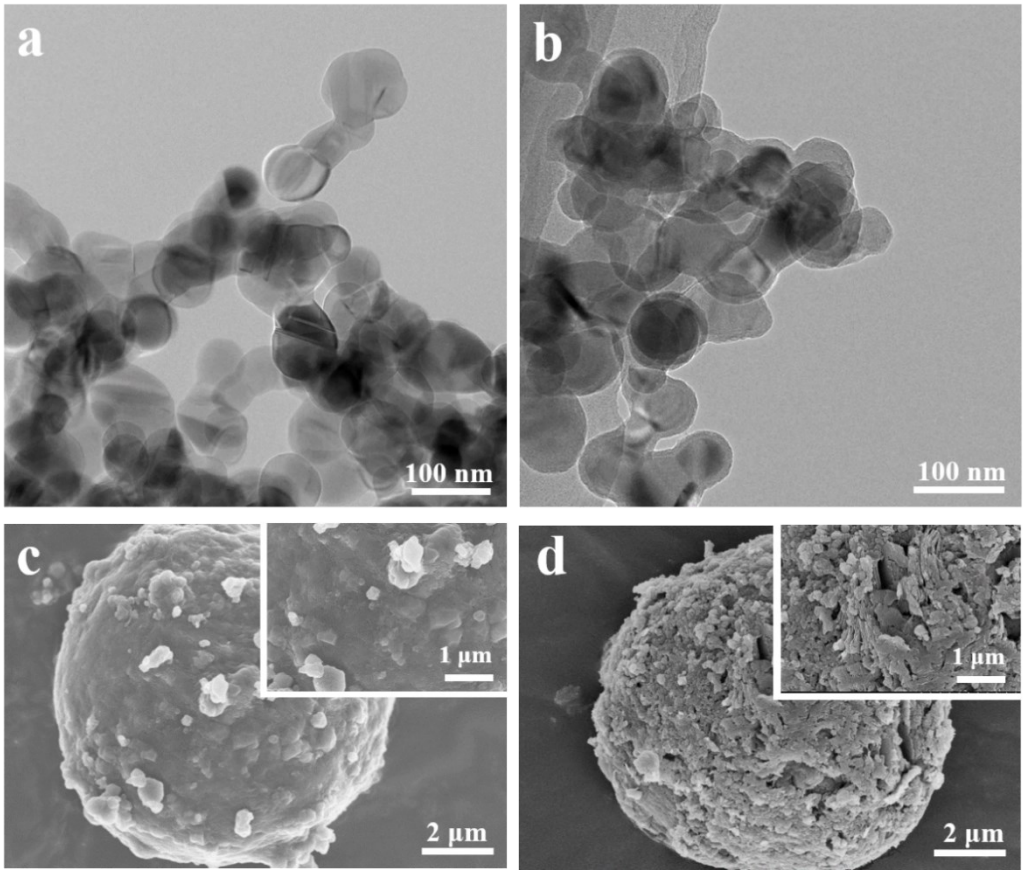

Figure S2 TEM images of (a) pure Si and (b) Si-PDDA. SEM images of (c) graphite and (d) graphite after being treated by mixed acid. A polymer layer is observed for Si-PDDA particles, indicating the successful modification of Si NPs by PDDA. After mixed acid oxidation, the graphite shows a relatively rough surface, which was generated by the positively charged Si-PDDA and negatively charged graphite through electrostatic attraction.

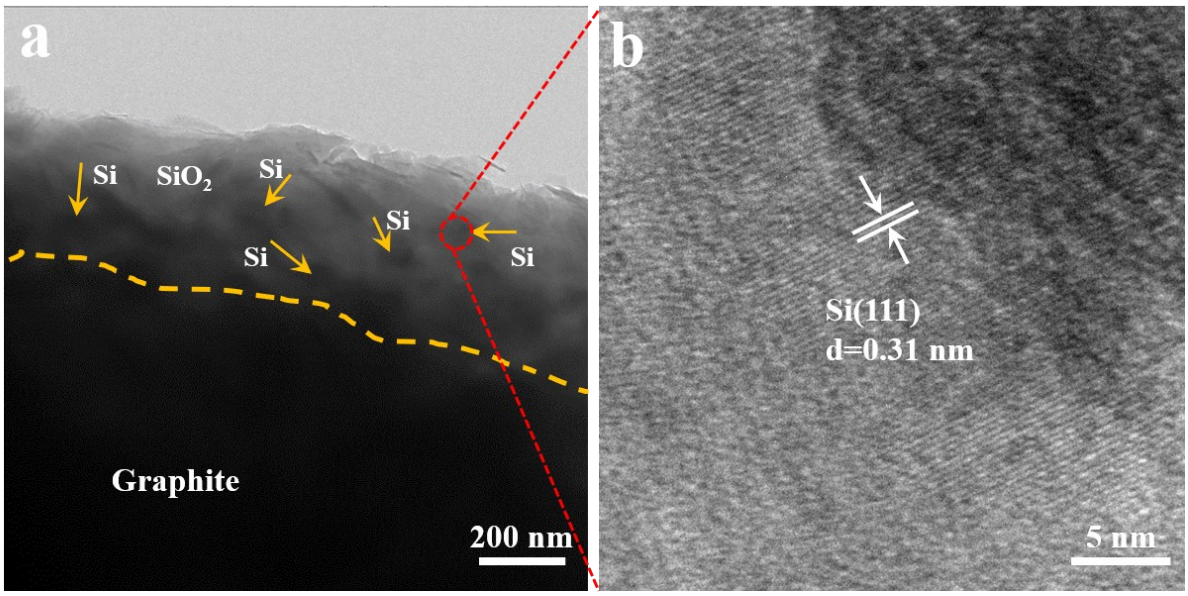

Figure S3 (a) TEM and (b) HRTEM images of G/Si/SiO_2 layer. The TEM images in Figure S3 further verify that the crystalline SiNPs are well encapsulated in the SiO_2 matrix with a thickness of about 400 nm deposited on the graphite skeleton.

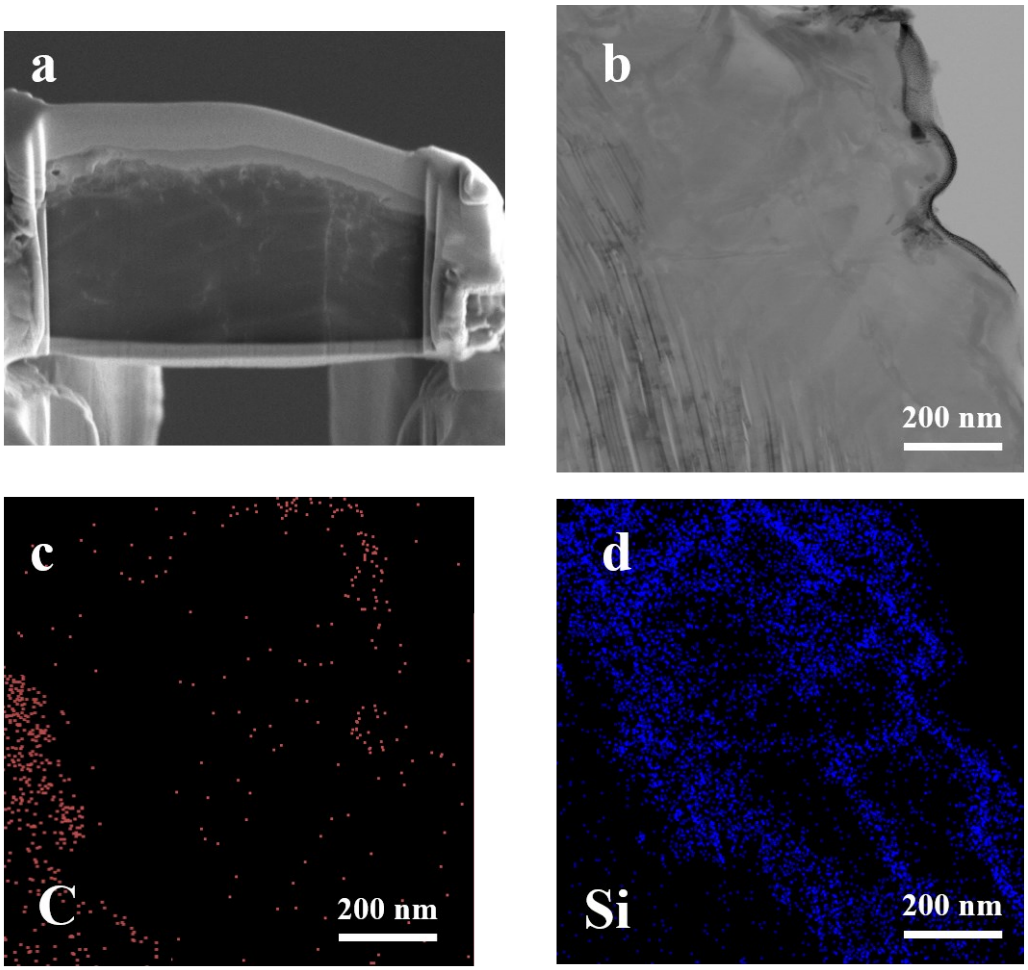

Figure S4 (a) SEM image, (b) TEM and (c and d) EDS of G@Si/SiO_2 layer/C in cross-sectional view.

TEM and corresponding EDS images are conducted after cutting the G@Si/SiO_2 layer/C by Dual-Beam Focus Ion Beam System (FIB). It can be seen that the carbon shell on the outmost layer of the G@Si/SiO_2 layer/C microsphere is isolated from the inner graphite core.

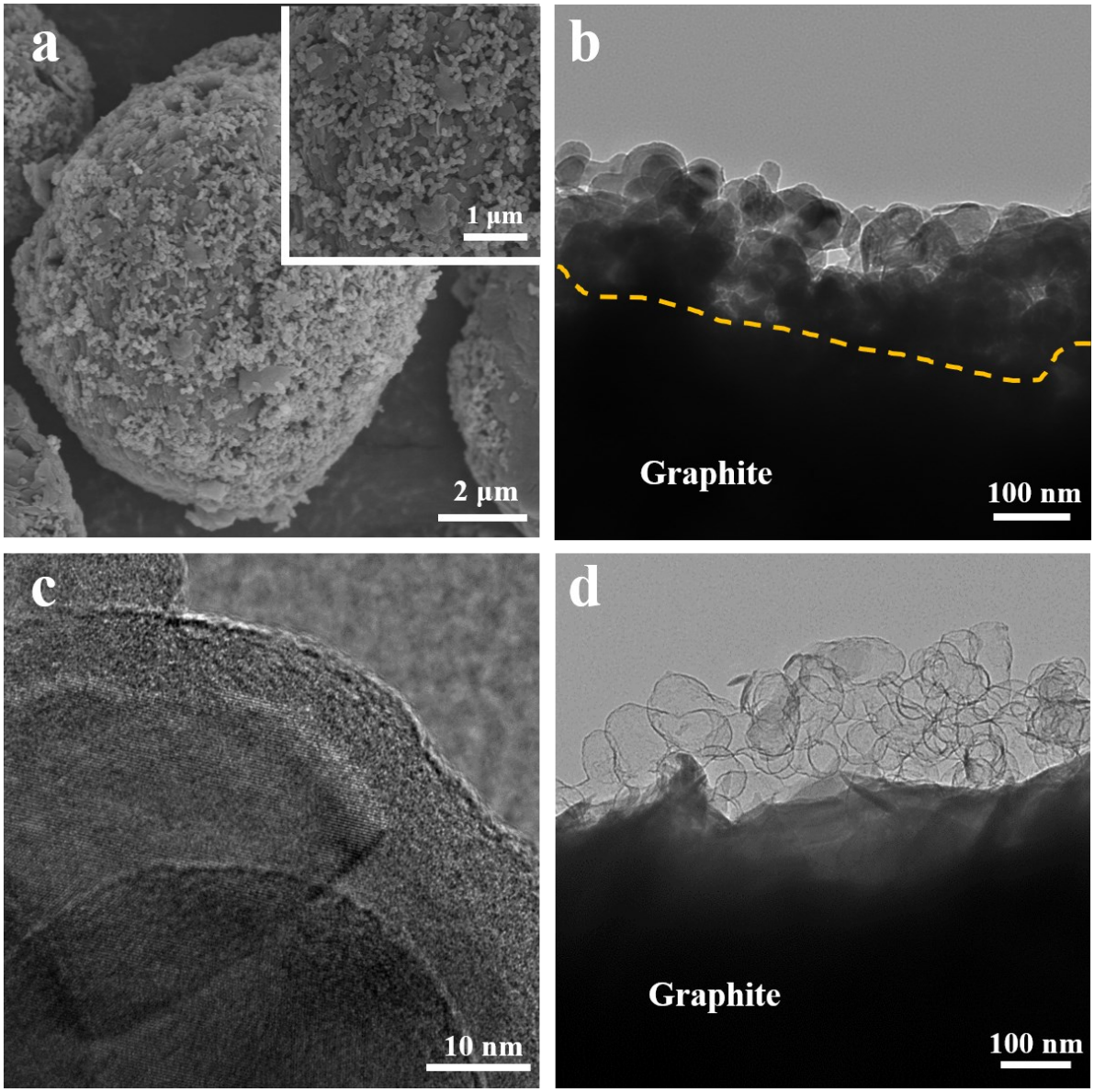

Figure S5 (a) SEM image of G@Si/C. (b) TEM and (c) HRTEM images of G@Si/C. (d) TEM image of G@Si/C after removing Si.

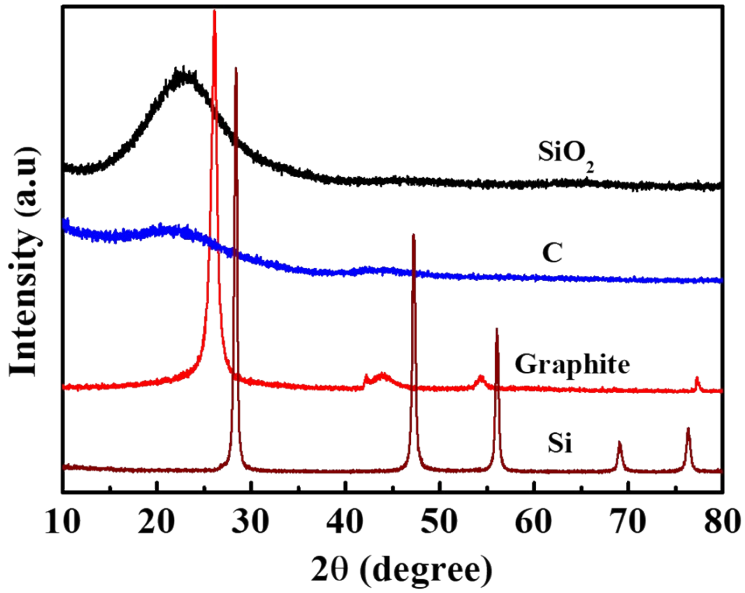

Figure S6 XRD patterns of SiO_2, amorphous carbon, graphite and Si.

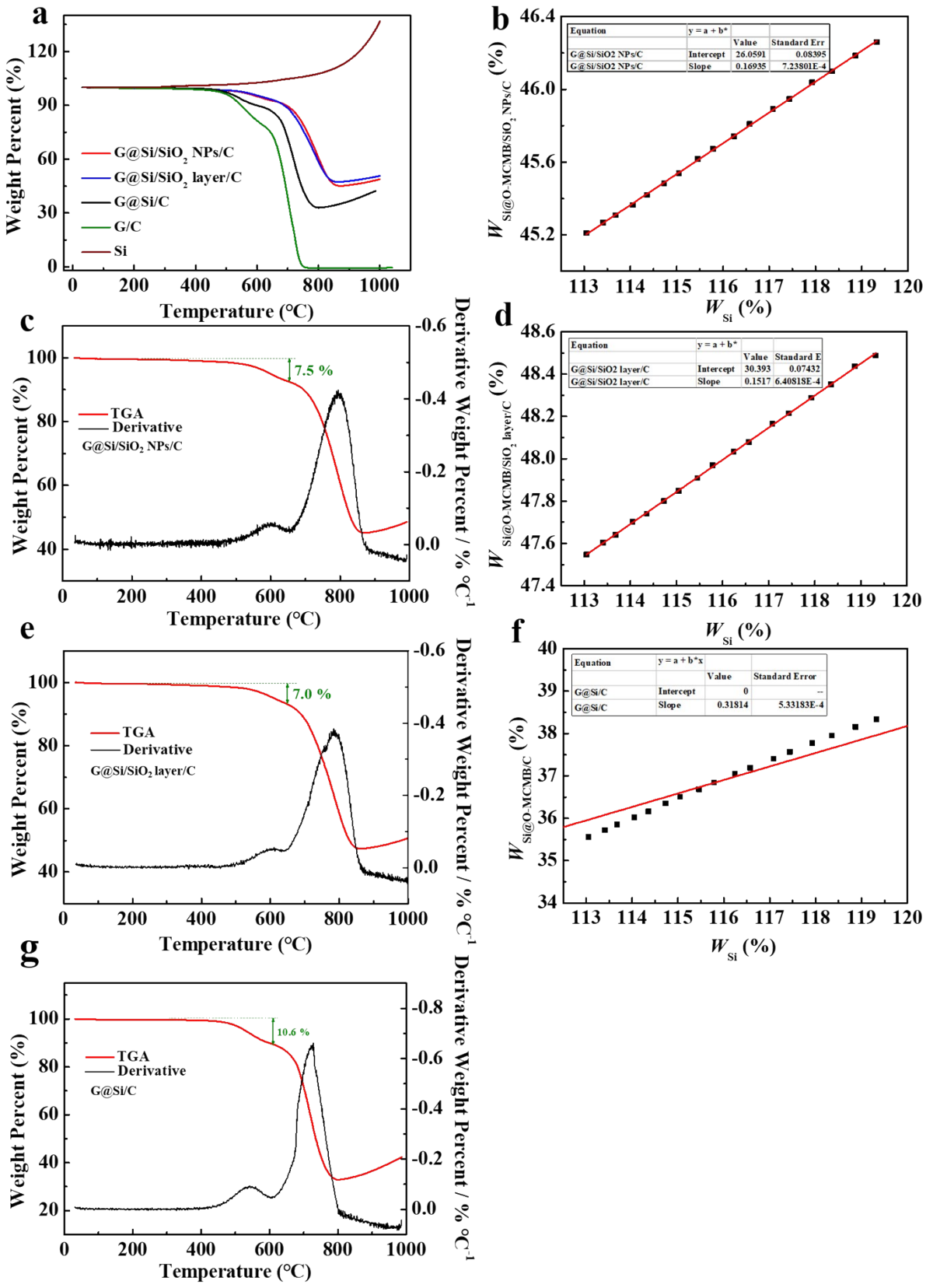

Figure S7 (a) Thermal gravimetric analysis (TGA) curves under the oxygen atmosphere at a heating rate of 10 °C min^{-1}. The relationship between remaining weight percent of (b) G@Si/SiO_2 NPs/C, (d) G@Si/SiO_2 layer/C and (f) G@Si/C, respectively. Weight percent and

derivative weight percentage curves for (c) G@Si/SiO_2 NPs/C, (e) G@Si/SiO_2 layer/C and (g) G@Si/C.

Note: The content of Si and SiO_2 in these composites could be calculated based on the equation: $W_{Si}x_{Si}+W_{graphite/C}(1-x_{Si}-x_{SiO2})+ W_{SiO2}=W_{G@Si/SiO2\ NPs/C}$ ($W_{G@Si/SiO2\ layer/C}$ or $W_{G@Si/C}$), where W_{Si}, $W_{G/C}$ and $W_{G@Si/SiO2\ NPs/C}$ ($W_{G@Si/SiO2\ layer/C}$ or $W_{G@Si/C}$) represent the remaining weight percent of SiNPs, G/C composites and G@Si/SiO_2 NPs/C (G@Si/SiO_2 layer/C or G@Si/C) composites, W_{SiO2} is the remaining weight percent of SiO_2, which is constant in all the test temperature ranges, x_{Si} denotes the content of Si. If the G/C combusts completely, in other words, $W_{G/C}$ is equal to 0, x_{si} and W_{SiO2} can be obtained from the slopes and intercept of W_{Si} vs. $W_{G@Si/SiO2\ NPs/C}$, $W_{G@Si/SiO2\ layer/C}$ or $W_{G@Si/C}$. The linear fitting between W_{Si} and $W_{G@Si/SiO2\ NPs/C}$, $W_{G@Si/SiO2\ layer/C}$ or $W_{G@Si/C}$ in the range of 880−930 °C are shown in Figure S6b, d and f. Accordingly, the content of Si and SiO_2 in the G@Si/SiO_2 NPs/C are determined to be 16.9% and 26.1% respectively, while that in the G@Si/SiO_2 layer/C hybrid spheres are 15.2% and 30.4%. In addition, the Si content of the G@Si/C is about 31.8%.

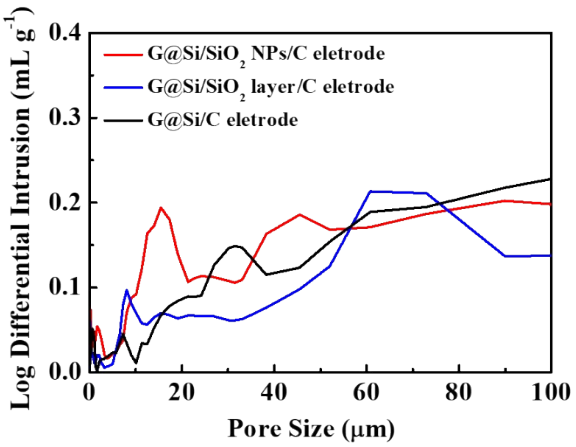

Figure S8 Pore size distribution curves of the different electrodes obtained with MIP.

Mercury intrusion porosimetry (MIP) is used to characterize the pore structures of the as made electrodes. Figure S8 shows that all electrodes have a broad pore size distribution, ranging from about 10 nm to several hundred micrometers. The results of porosity and average pore diameter from MIP are summarized in Table S2. The higher overall porosity and larger pore size are conducive to the fast wetting of the electrodes

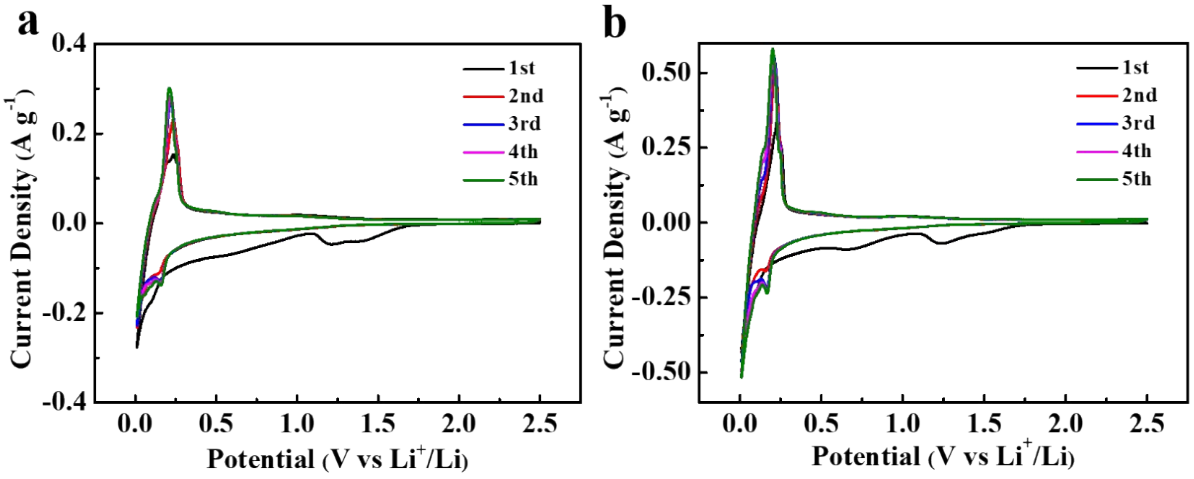

Figure S9 Cyclic voltammetry profiles of (a) G@Si/SiO_2 layer/C and (b) G@Si/C.

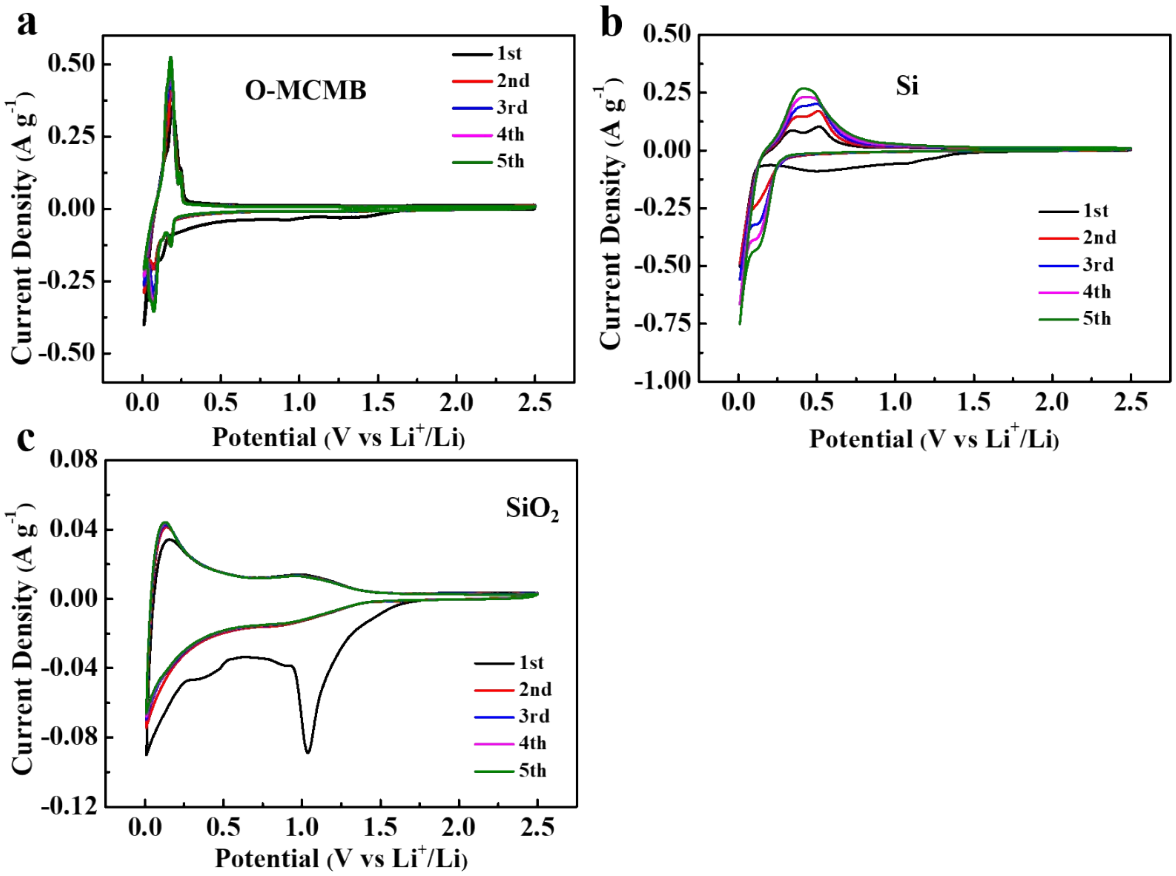

Figure S10 Cyclic voltammetry profiles of (a) graphite, (b) Si and (c) pure SiO_2 electrodes.

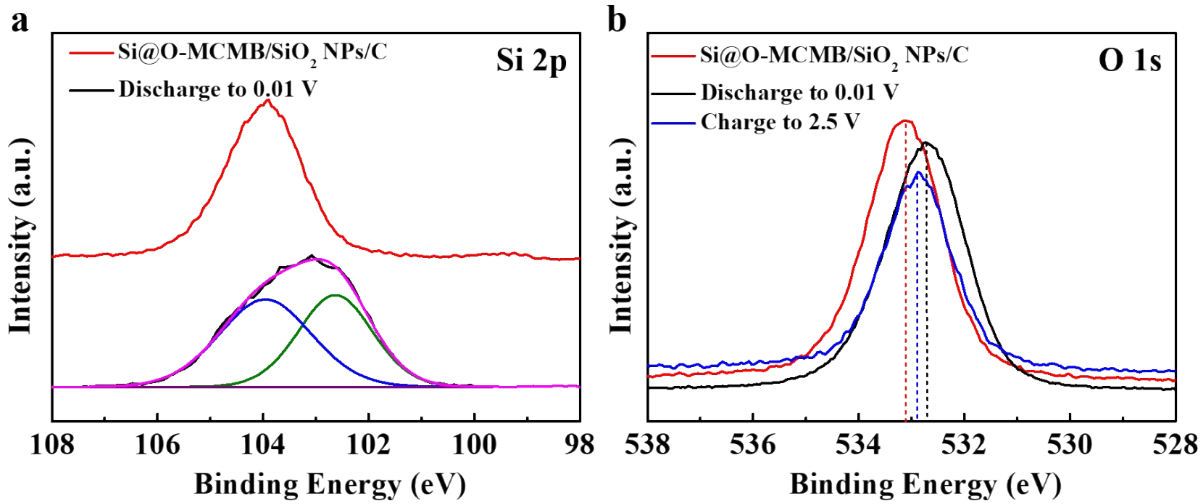

Figure S11 The Si 2p (a) and O 1s (b) XPS spectra of the G@Si/SiO_2 NPs/C before and after cycle.

X-ray photoelectron spectroscopy (XPS) was employed to check the variation of the crystalline structure of SiO_2 during the electrochemical process. As shown in Figure S11, the peak at 103.9 eV is corresponding to the amorphous silica. After discharge, two new peaks appear, the one located at 103.4 eV is assigned to Li_4SiO_4 and the other at 102.0 eV belongs to Li−Si alloy. As expected, the O 1s peak also shifts to low binding energy after discharge. In addition, the peak of O 1s does not fully recover to its previous position, which means that the formation of the Li_4SiO_4 is irreversible.

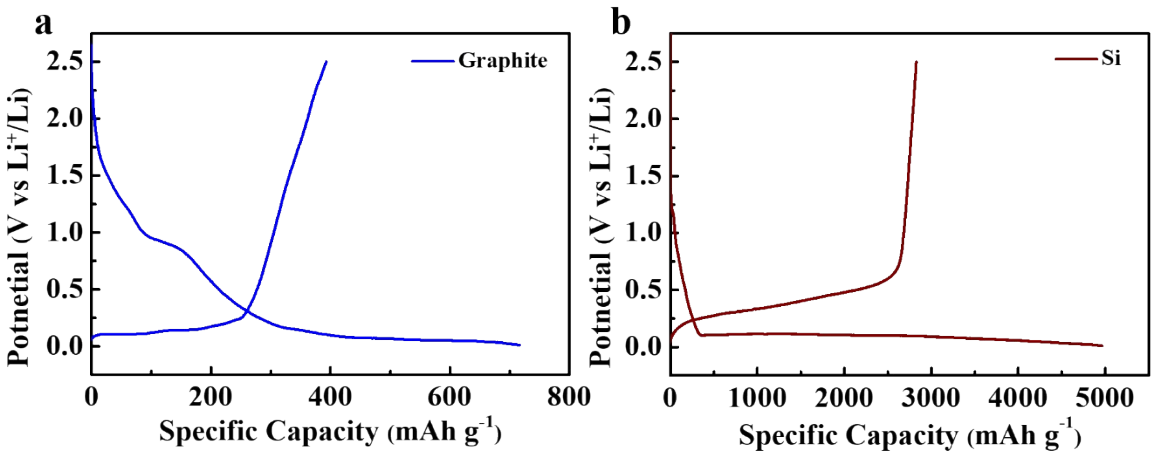

Figure S12 Initial discharge-charge voltage profiles of (a) graphite after treated with mixed acid and (b) Si.

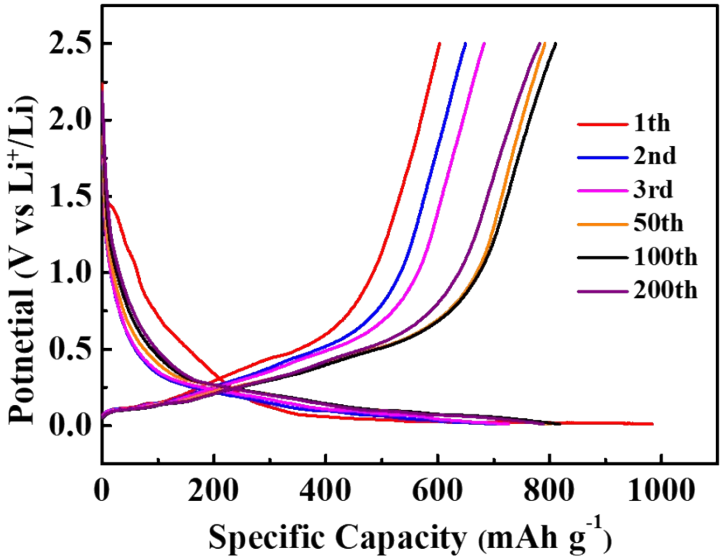

Figure S13 Voltage profiles of the G@Si/SiO_2 NPs/C composites for the 1st, 2nd, 3rd, 50th, 100th, and 200th cycles.

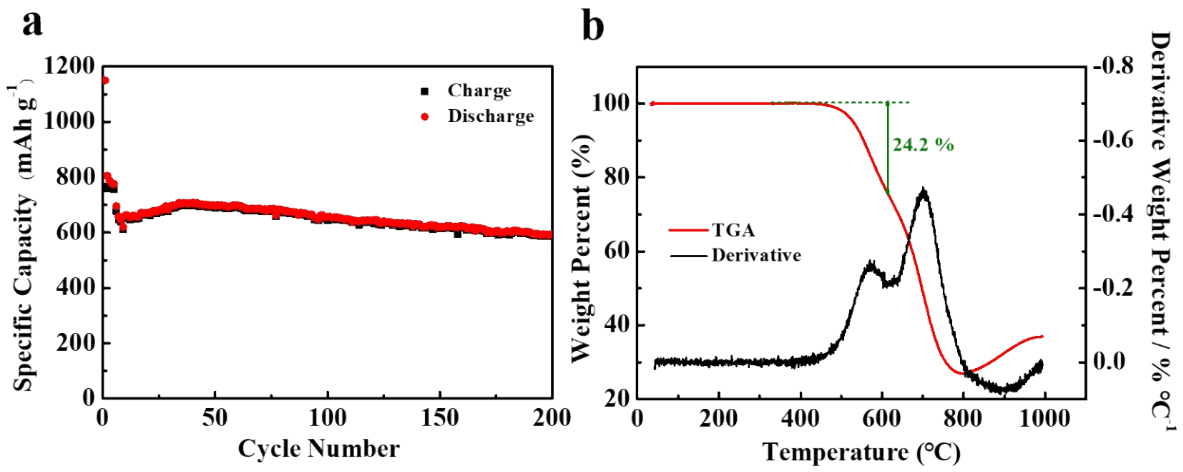

Figure S14 (a) Cycling performance of G@Si/C with a high carbon content of 24.2%. (b) The weight percent and derivative weight percentage curves.

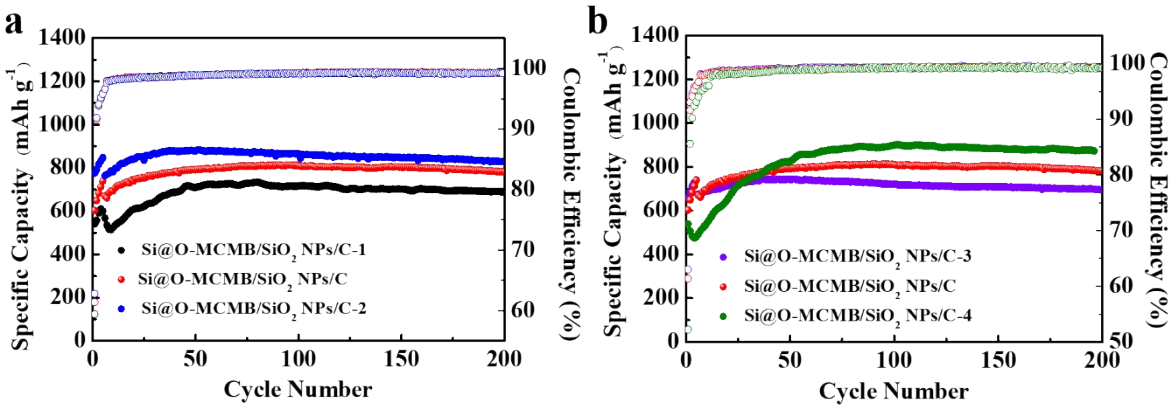

Figure S15 Cycling performances of G@Si/SiO_2 NPs/C with different components.

The G@Si/SiO_2 NPs/C composites with different components are also prepared (Figure S16 and Table S1). When increasing the amount of Si, the G@Si/SiO_2 NPs/C-2 composites show a higher specific capacity of 884 mAh g^{-1} and a slightly more rapid capacity fading at 200 mA g^{-1} compared to the G@Si/SiO_2 NPs/C and G@Si/SiO_2 NPs/C-1 composites with the lower amount of Si (Figure S15 a).

As increasing the amount of SiO_2, the specific capacity of G@Si/SiO_2 NPs/C-4 increases to 891 mAh g^{-1} and the capacity retention is almost 100% after 200 cycles. While too much SiO_2 and too little amorphous carbon prolong the activation time (Figure S15 b).

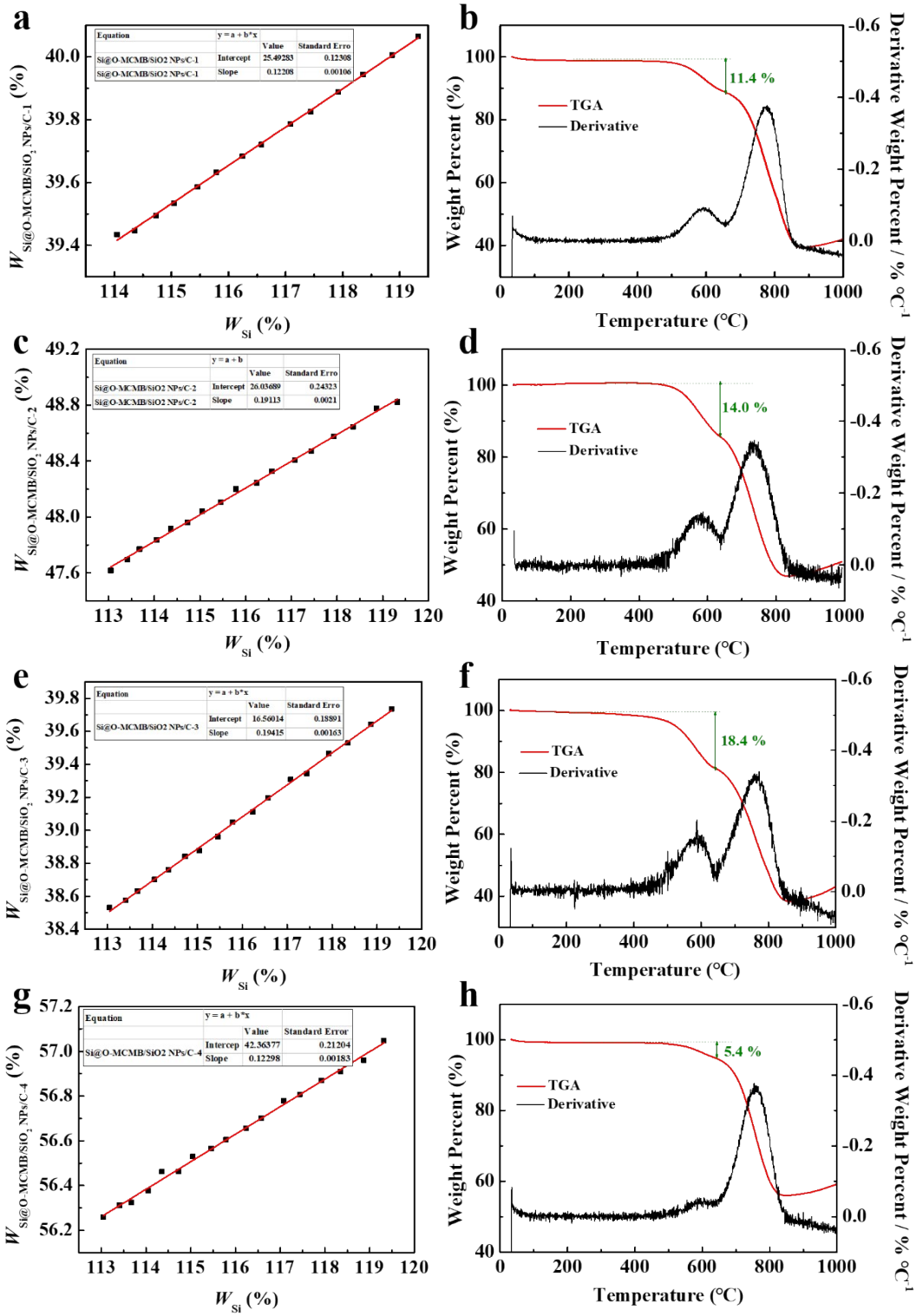

Figure S16 The relationship between remaining weight percent of (a) G@Si/SiO_2 NPs/C-1, (c) G@Si/SiO_2 NPs/C-2, (e) G@Si/SiO_2 NPs/C-3 and (g) G@Si/SiO_2 NPs/C-4, respectively. Weight percent and derivative weight percentage curves for (d) G@Si/SiO_2 NPs/C-1, (e) G@Si/SiO_2 NPs/C-2, (f) G@Si/SiO_2 NPs/C-3 and (h) G@Si/SiO_2 NPs/C-4.

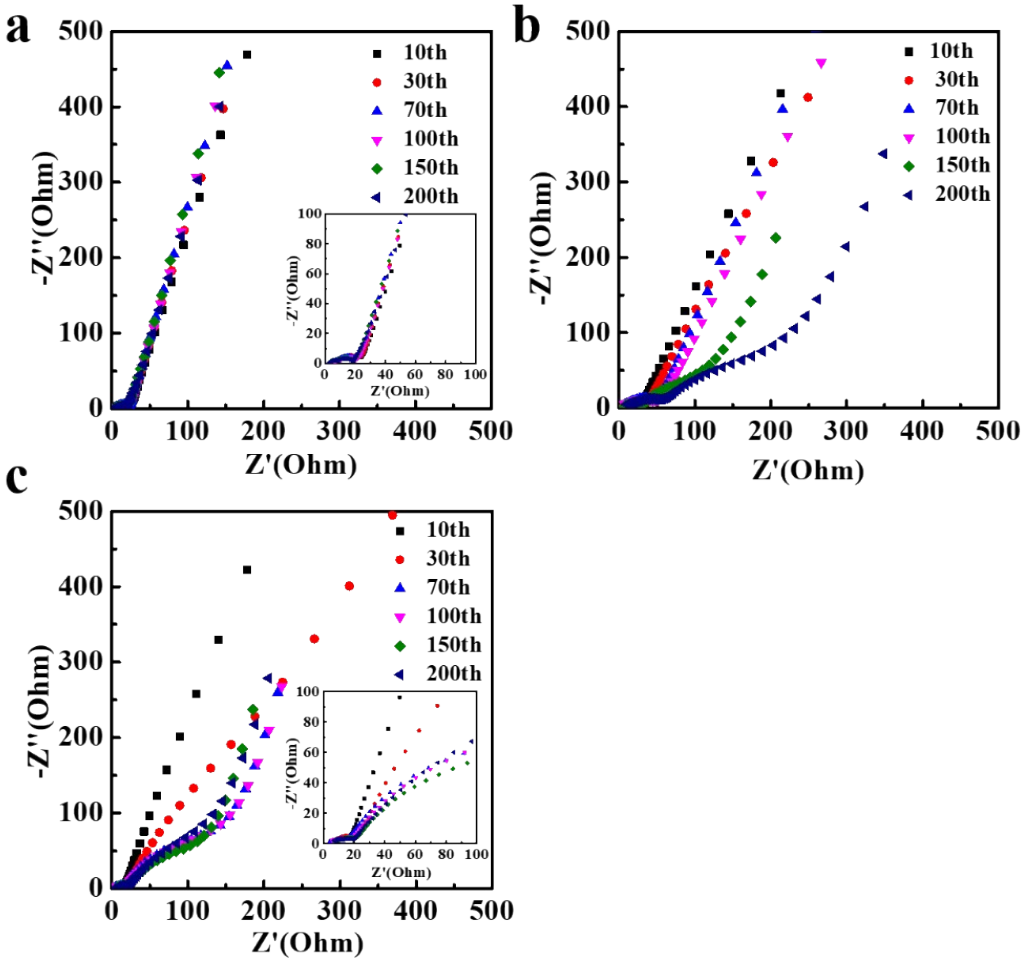

Figure S17 Nyquist plots of the EIS spectra of the (a) G@Si/SiO_2 NPs/C, (b) G@Si/SiO_2 layer/C and (c) G@Si/C electrodes in the delithiation stage after different cycles at 0.5 A g^{-1}.

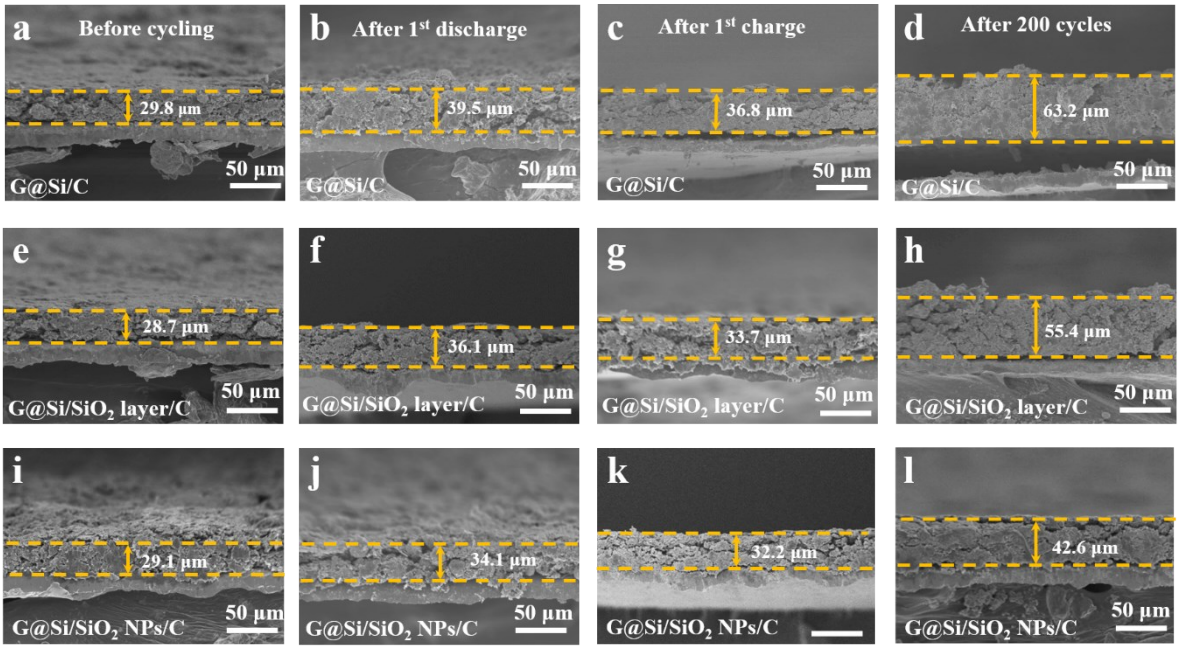

Figure S18 Cross-sectional SEM images of G@Si/C electrodes (a) before cycles, (b) after 1st discharge, (c) after 1st charge and (d) after 200th charge. Cross-sectional SEM images of G@Si/SiO_2 layer/C electrodes (e) before cycles, f) after 1st discharge, (g) after 1st charge and (k) after 200th charge. Cross-sectional SEM images of G@Si/SiO_2 NPs/C electrodes (i) before cycles, (j) after 1st discharge, (k) after 1st charge and (l) after 200th charge.

After first discharge, the G@Si/SiO_2 NPs/C anode with a thickness of 29.1 μm expands to about 17.2% (34.1 μm) in height, which is much lower than 25.8% for G@Si/SiO_2 layer/C and 32.6% for G@Si/C electrodes. After a subsequent charge process, the thickness of the G@Si/SiO_2 NPs/C composite anode slightly decreased to 32.2 μm, corresponding to 10.7%, which is also a lower value compared with the 17.4% of the G@Si/SiO_2 layer/C and 23.5% of the G@Si/C anode. After a long cycle (200 cycles at the charge state), the G@Si/C electrode exhibits a large thickness increase of 112% with particles delamination. While the G@Si/SiO_2 NPs/C shows the smallest volume expansion (46%) with no obvious variation of the electrode surface after cycles, implying that the conformal coated carbon on SiO_2 NPs in the G@Si/SiO_2 NPs/C can tolerate the volume expansion more effectively than outermost carbon layer in G@Si/SiO_2 layer/C during the lithiation/delithiation process, thereby retaining structural stability after long cycling.

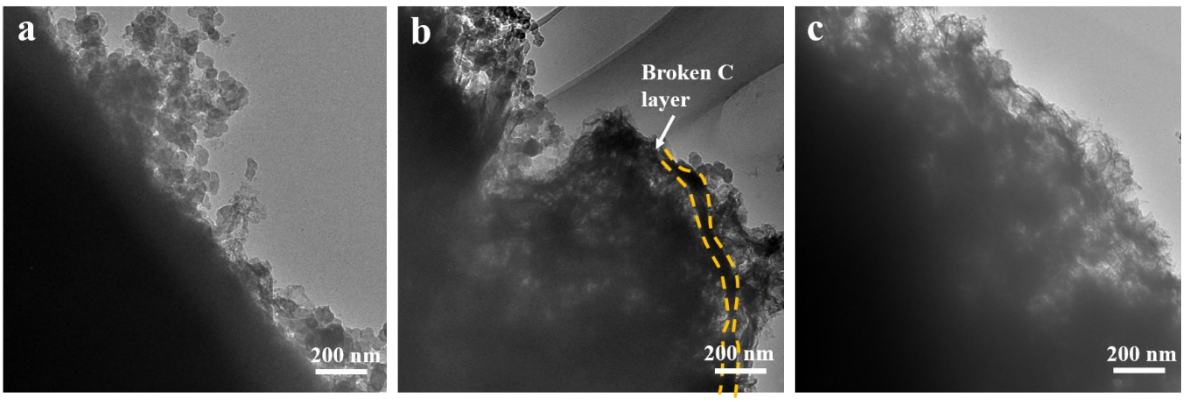

Figure S19 TEM of the (a) G@Si/C, (b) G@Si/SiO_2 layer/C and (c) G@Si/SiO_2 NPs/C electrodes after 200 cycles at 0.5 A g^{-1}.

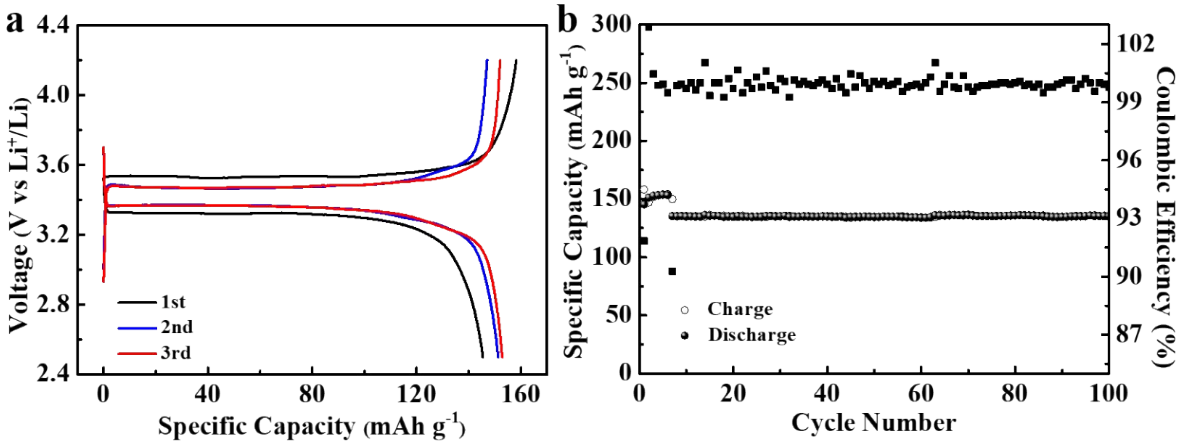

Figure S20 (a) Voltage profiles of LFP half cells. (b) The Cycling performance of the LFP half cells tested at 0.2 C for the first five cycles and 1 C for the later cycles.

Table S1. Thermogravimetric analysis of G@Si/SiO_2 NPs/C, G@Si/SiO_2 layer/C and G@Si/C composites.

	Si (wt.%)	SiO_2 (wt.%)	graphite (wt.%)	C (wt.%)
G@Si/SiO_2 NPs/C	16.9	26.1	49.3	7.5
G@Si/SiO_2 layer/C	15.2	30.4	47.4	7.0
G@Si/C	31.8	0	57.6	10.6
G@Si/SiO_2 NPs/C-1	12.2	25.5	50.9	11.4
G@Si/SiO_2 NPs/C-2	19.1	26.0	40.8	14.0
G@Si/SiO_2 NPs/C-3	19.6	16.4	45.6	18.4
G@Si/SiO_2 NPs/C-4	12.3	42.4	39.9	5.4

Table S2. Results summary for total intrusion volume, average pore diameter and porosity from mercury intrusion porosimetry (MIP).

	Total Intrusion Volume ($mL\ g^{-1}$)	**Average Pore Diameter (nm)**	**Porosity (%)**
G@Si/SiO_2 NPs/C	0.4542	121.3	52.6
G@Si/SiO_2 layer/C	0.3311	155.4	46.3
G@Si/C	0.6258	168.6	56.4

Table S3. Electrochemical performances comparison of Si-graphite anode materials in LIBs.

Materials	Current ($A\ g^{-1}$)	Capacity ($mAh\ g^{-1}$)	Cycle Number	Retention (%)	Ref.
G@Si/SiO2 NPs/C	**0.2**	**~800**	**200**	**96**	**This work**
	0.5	**~600**	**800**	**92**	
G@Si/SiO2 layer/C	**0.2**	**~800**	**200**	**88**	
Si-nanolayer-embedded graphite/carbon	0.25	~500	100	96	1
Si/carbon/graphite	0.13	568	100	83.8	2
Si@O-MCMB/C	0.1	560	200	92.8	3
MCMB@Si@C	0.1	632	100	91.1	4
SGCpitch	0.25	523	50	97.5	5
Si/graphite/pyrolytic carbon	0.5	610	300	83.6	6
Silicon/carbon/natural graphite	0.1	471.5	100	87.9	7
Polymer-carbon coated Si-on-graphite	0.09	480	200	95	8
Si/pyrolyzed carbon@ graphite	0.1	550	100	93.75	9
Si/graphite/carbon	1	640	50	87.6	10
Si/C microspheres	0.3	~600	500	83.3	11

Reference

1. M. Ko, S. Chae, J. Ma, N. Kim, H.-W. Lee, Y. Cui and J. Cho, Scalable synthesis of silicon-nanolayer-embedded graphite for high-energy lithium-ion batteries, *Nat. Energy*, 2016, **1**, 16113-16121.

2. S.Y. Kim, J. Lee, B.H. Kim, Y.J. Kim, K.S. Yang and M.S. Park, Facile Synthesis of Carbon-Coated Silicon/Graphite Spherical Composites for High-Performance Lithium-Ion Batteries, *ACS Appl. Mater. Interfaces*, 2016, **8**, 12109-12117.

3. H. Liu, Z. Shan, W. Huang, D. Wang, Z. Lin, Z. Cao, P. Chen, S. Meng and L. Chen, Self-Assembly of Silicon@Oxidized Mesocarbon Microbeads Encapsulated in Carbon as Anode Material for Lithium-Ion Batteries, *ACS Appl. Mater. Interfaces*, 2018, **10**, 4715-4725.

4. Y. Lin, Y. Chen, Y. Zhang, J. Jiang, Y. He, Y. Lei, N. Du and D. Yang, Wet-chemical synthesized MCMB@ Si@ C microspheres for high-performance lithium-ion battery anodes, *Chem. Commun.*, 2018, **54**, 9466-9469.

5. S.-H. Choi, G. Nam, S. Chae, D. Kim, N. Kim, W.S. Kim, J. Ma, J. Sung, S.M. Han, M. Ko, H.-W. Lee and J. Cho, Robust Pitch on Silicon Nanolayer-Embedded Graphite for Suppressing Undesirable Volume Expansion, *Adv. Energy Mater.*, 2019, **9**, 1803121-1803131.

6. D. Sui, Y. Xie, W. Zhao, H. Zhang, Y. Zhou, X. Qin, Y. Ma, Y. Yang and Y. Chen, A high-performance ternary Si composite anode material with crystal graphite core and amorphous carbon shell, *J. Power Sources*, 2018, **384**, 328-333.

7. A. Wang, F. Liu, Z. Wang and X. Liu, Self-assembly of silicon/carbon hybrids and natural graphite as anode materials for lithium-ion batteries, *RSC Adv.*, 2016, **6**, 104995-105002

8. F. S. Li, Y. S. Wu, J. Chou and N. L. Wu, A dimensionally stable and fast-discharging graphite–silicon composite Li-ion battery anode enabled by electrostatically self-assembled multifunctional polymer-blend coating, *Chem. Commun.*, 2015, **51**, 8429-8431.

9. Z. Wang, Z. Mao, L. Lai, M. Okubo, Y. Song, Y. Zhou, X. Liu and W. Huang, Sub-micron silicon/pyrolyzed carbon@ natural graphite self-assembly composite anode material for lithium-ion batteries, *Chem. Engi. J.*, 2017, **313**, 187-196.

10. C. Xiao, P. He, J. Ren, M. Yue, Y. Huang and X. He, Walnut-structure Si–G/C materials with high coulombic efficiency for long-life lithium ion batteries, *RSC Adv.*, 2018, **8**, 27580-27586.

11. Q. Xu, J.-Y. Li, J.-K. Sun, Y.-X. Yin, L.-J. Wan and Y.-G. Guo, Watermelon-Inspired Si/C Microspheres with Hierarchical Buffer Structures for Densely Compacted Lithium-Ion Battery Anodes, *Adv. Energy Mater.*, 2017, **7**, 1601481-1601488.